Lab on a Chip

Cite this: *Lab Chip*, 2012, **12**, 4433–4440

www.rsc.org/loc

PAPER

Integrated capture, transport, and magneto-mechanical resonant sensing of superparamagnetic microbeads using magnetic domain walls

E. Rapoport, D. Montana and G. S. D. Beach*

Received 7th April 2012, Accepted 20th August 2012
DOI: 10.1039/c2lc40715a

An integrated platform for the capture, transport, and detection of individual superparamagnetic microbeads is described for lab-on-a-chip biomedical applications. Magnetic domain walls in magnetic tracks have previously been shown to be capable of capturing and transporting individual beads through a fluid at high speeds. Here it is shown that the strong magnetostatic interaction between a bead and a domain wall leads to a distinct magneto-mechanical resonance that reflects the susceptibility and hydrodynamic size of the trapped bead. Numerical and analytical modeling is used to quantitatively explain this resonance, and the magneto-mechanical resonant response under sinusoidal drive is experimentally characterized both optically and electrically. The observed bead resonance presents a new mechanism for microbead sensing and metrology. The dual functionality of domain walls as both bead carriers and sensors is a promising platform for the development of lab-on-a-bead technologies.

1 Introduction

Surface-functionalized superparamagnetic (SPM) microbeads are widely used to tag, manipulate, and detect chemical and biological species in a fluid environment. There is great interest in exploiting this functionality in chip-based devices[1–26] that reduce the complexity, time, and volume of material required for chemical or biological analysis in, *e.g.*, rapid medical screening applications. Recent work has shown that, owing to their highly localized stray fields, magnetic domain walls (DWs) in magnetic nanotracks can be used to shuttle individual SPM microbeads and magnetically tagged entities across the surface of a substrate.[17–23,26] By integrating a single-bead detection mechanism into such DW-based transport structures, microscale sorting and sensing of single cells or biomolecules could be simultaneously achieved in magnetic lab-on-a-chip devices.

Magnetoresistive sensors, which exhibit a perturbed response to applied excitation fields due to the presence of beads at the sensor surface,[1–3,13–17] form the basis for most SPM bead sensing platforms. On-chip bead-based sensing of biomolecules with such devices usually relies on chemical functionalization of the sensor surface for preferential capture and immobilization of magnetic marker beads that bind the chemical target in the host fluid. This mode of sensing precludes subsequent transport of immobilized beads, and requires chemical decoration of the sensors, which adds complexity to device fabrication. Brownian relaxation biodetection[24,25,27–32] instead uses the beads themselves as the capture agent and thus does not require chemical immobilization of beads on the sensor surface. The Brownian relaxation frequency is directly related to the hydrodynamic radius of the beads, such that changes in the radius due to target binding at the bead surface manifest as a shift in the relaxation frequency. Dalslet *et al.*[24] and Donolato *et al.*[25] have recently demonstrated on-chip detection of beads suspended in a fluid above a magnetoresistive sensor based on their Brownian relaxation. However, sensitivity at the level of individual microbeads has not yet been demonstrated using such a mechanism.

Domain walls in nanotracks can be used to reversibly capture and transport SPM microbeads,[17–23,26] and it was recently shown that DWs can also be used to sense the presence of individual beads.[13,17,26] Llandro *et al.*[13] demonstrated the detection of individual beads by measuring the effect of their stray field on DW-mediated magnetization switching in pseudo-spin-valves.[33] Vavassori *et al.*[17] exploited the magnetic focusing action of DWs to position a bead near a DW trapped at a nanotrack corner, and then detect the bead's presence based on a small change in the DW depinning field. However, both of these mechanisms rely on sensing small changes to the switching field, which itself is typically stochastic in nature. Moreover, the use of these mechanisms for biomolecular sensing would still require chemical hybridization between the beads and the sensor surface to indicate the presence of a target analyte, and is therefore incompatible with simultaneous DW-based bead transport.

Here we show that a SPM bead trapped by a DW exhibits a distinct magneto-mechanical resonance that depends on its hydrodynamic characteristics in the host fluid. By measuring the mechanical response of a bead trapped by a sinusoidally driven DW, we show that a characteristic resonant frequency

Department of Materials Science and Engineering, Massachusetts Institute of Technology, Cambridge, Massachusetts, 02139, USA.
E-mail: gbeach@mit.edu

exists that is a function of the bead size and the strength of its interaction with the DW. We demonstrate size-based discrimination amongst commercial microbead populations based on this mechanism, and develop a device structure and methodology whereby the resonance can be measured electrically in a DW transport conduit. This magneto-mechanical resonance offers a means to distinguish single beads based on their physical characteristics, and could hence be exploited to allow DW-based devices to trap, sense, transport, and release individual magnetic beads in one integrated system.

2 Theory

2.1 Magnetic bead-DW interaction

We consider a SPM bead proximate to a submicrometer-wide track of soft magnetic material. In such a track, magnetic domains orient along the length, separated by DWs that generate high-gradient stray magnetic fields, $\boldsymbol{B}(\boldsymbol{r})$, due to the strong divergence of the DW magnetization. The DW stray field induces a magnetic moment in a nearby SPM bead, creating a localized magnetostatic potential well. This well acts as a trap that can be used to manipulate individual beads, and bead transport has been realized by either stepping a bead from one fixed DW trap site to the next[18,19,21,22] or moving it continuously with a propagating DW.[19,22,23,26] The maximum transport speed is determined by the strength of the bead-DW magnetostatic interaction, which must overcome the hydrodynamic drag on the bead as it is pulled through the host fluid. Previously, we have shown that this interaction leads to a strong restoring force F_{int} (Fig. 1c), that can enable transport at speeds approaching 1 mm s^{-1}.[23] Here we will show that the form of this interaction potential leads to resonant coupled dynamics that can be used to distinguish individual beads based on their size.

We have calculated the magnetostatic potential energy landscape for SPM beads near a DW in a magnetic nanotrack using parameters appropriate to the experiments described below. Fig. 1c, inset shows the top-down view of the spin configuration in the x-y plane of a head-to-head DW in a 800 nm wide, 40 nm thick $Ni_{80}Fe_{20}$ (Permalloy) track, computed micromagnetically using the Object-Oriented Micromagnetics Framework (OOMMF) platform.[34] The simulation assumed materials parameters for bulk $Ni_{80}Fe_{20}$ (exchange constant A = 1.3 × 10^{-11} J m^{-1}, saturation magnetization M_s = 800 kA m^{-1}, uniaxial anisotropy K_u = 0), and used a cell size of 5 × 5 × 40 nm^3. The simulated DW exhibits a vortex structure as expected for these dimensions.[35] The magnetization profile was used to compute the stray field *via* the scalar potential. From the stray field, the magnetostatic potential energy of a spherical SPM bead was estimated by integrating the dipolar energy density $-\boldsymbol{M}\cdot\boldsymbol{B}$ over the bead volume, assuming a bead magnetization $\boldsymbol{M} = \chi\boldsymbol{B}/\mu_0$ with χ = 800 kA m^{-1} T^{-1}.[9]

Fig. 1a, b shows the calculated potential energy wells for bead sizes (2.8 μm and 1.0 μm diameter) used in experiment. The energy surface for a 2.8 μm diameter bead is very well approximated by a parabolic harmonic potential (Fig. 1a, inset), such that the bead-DW restoring force F_{int}, calculated from the gradient of the energy surface, can be modeled as linear with force constant k for small relative displacements between the DW and trapped bead. For the smaller 1.0 μm diameter bead, whose potential landscape is more sensitive to local DW stray field variation (Fig. 1b), a parabolic approximation holds relatively well for displacements on the order of half the bead diameter or larger (Fig. 1b, inset).

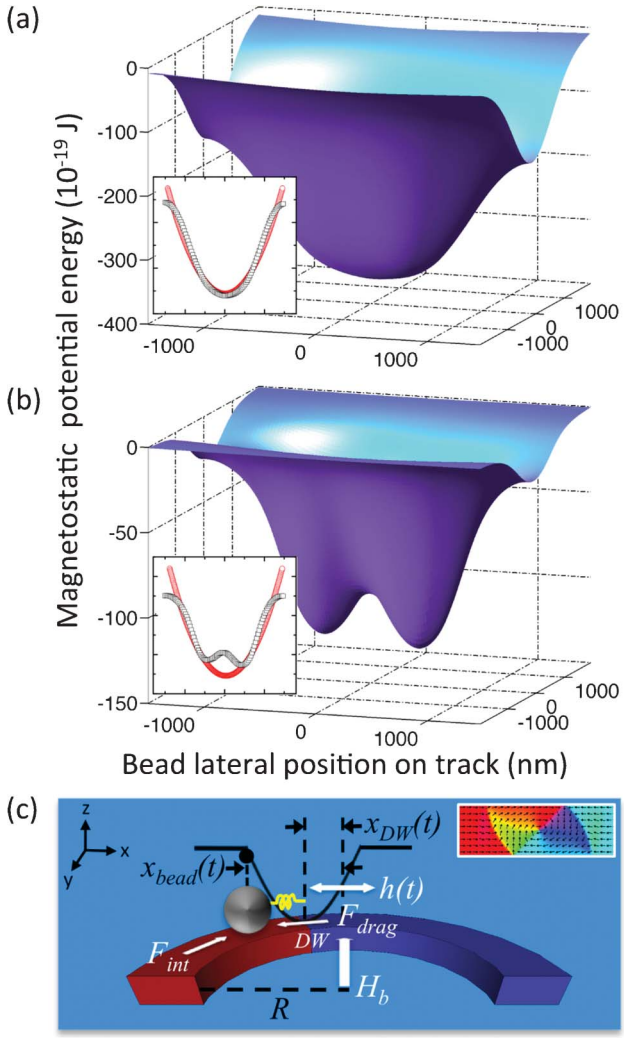

Fig. 1 Magnetostatic potential energy and resonance dynamics of bead-DW system. Magnetostatic potential energy *versus* lateral position for a (a) 2.8 μm diameter and (b) 1.0 μm diameter SPM bead at the surface of a 800 nm wide × 40 nm thick $Ni_{80}Fe_{20}$ track containing a vortex wall. Insets show longitudinal energy cross sections (squares) fitted to a harmonic potential (circles). (c) Schematic of the oscillator geometry in the bead-DW system with curvilinear track. The bead is tethered to the vortex DW (inset, showing the top-down view of spin configuration in the x-y plane) by a restoring force F_{int} arising from the magnetostatic interaction potential. The viscous drag force F_{drag} from the fluid on the bead resists bead motion.

2.2 Magneto-mechanical resonance

Because of its quasilinear restoring force, the coupled bead-DW system should behave as a harmonic mechanical oscillator. If the DW is driven sinusoidally about a fixed position at low frequency, the bead is expected to track the DW motion. However, at higher frequencies, the bead should lag behind the DW due to viscous drag, leading to a frequency-dependent phase shift between the motion of the two. Due to viscous damping in the fluid, the coupled system should thus exhibit an overdamped

resonant response to an external periodic excitation, with a characteristic resonance frequency dependent on the restoring force and the viscous drag.

We consider the curved track geometry of Fig. 1c, in which a DW is driven about a fixed position by a pair of orthogonal in-plane magnetic fields. A radial bias field $H_b\,\hat{\boldsymbol{y}}$ establishes the equilibrium DW position, while a tangential ac field $h(t)\boldsymbol{x}$ drives the DW sinusoidally about that position. As the DW is displaced by an angle φ from the $\hat{\boldsymbol{y}}$ axis, it experiences a force $-2\mu_0 M_s t w H_b \sin(\varphi)$ from the bias field proportional to the tangential projection of the field along the track. If the DW displacement x_{DW} along the track perimeter is small compared to the track radius R, then $\sin(\varphi) \approx x_{DW}/R$ and the bias field exerts a linear restoring force on the DW. In the absence of a trapped bead, the DW simply follows $x_{DW} = (h(t)/H_b)R$.

When an oscillating DW has trapped a SPM bead, its motion couples to that of the bead through a magnetostatic interaction *via* a force linear in their relative displacement, $k(x_{bead}-x_{DW})$.[36] Viscous drag from the fluid acts to resist the motion of the bead as it is dragged by the DW (Fig. 1c), leading to a damping term $F_{drag} = -b\frac{d}{dt}x_{bead}$, with b proportional to the radius of the bead and viscosity of the host fluid.

Assuming strongly overdamped conditions (*i.e.*, neglecting inertial terms), we hence arrive at a set of coupled equations of motion for the bead and DW coordinates $x_{bead}(t)$ and $x_{DW}(t)$,

$$-k(x_{bead}-x_{DW})-b\frac{d}{dt}x_{bead}=0 \tag{1a}$$

$$+k(x_{bead}-x_{DW})-\frac{CH_b}{R}x_{DW}+Ch(t)=0 \tag{1b}$$

where $C = 2\mu_0 M_s t w$. Eqn (1a) and eqn (1b) account for forces on the bead and DW, respectively. For a sinusoidal drive field $h(t) = h_0 e^{-i\omega t}$, these equations can be solved assuming a harmonic response from both the bead and DW, $x_{bead}(t) = \delta_{bead}e^{-i\omega t}$ and $x_{DW}(t) = \delta_{DW}e^{-i\omega t}$, where δ_{bead} and δ_{DW} are the complex oscillation amplitudes of the bead and DW, respectively.

In the dc limit, the bead and DW move in unison, following the driving field with a displacement amplitude $\delta^0_{bead} = \delta^0_{DW} = Rh_0/H_b$. At higher frequencies, viscous drag causes the bead to lag behind the DW, resulting in an overdamped resonant response given by

$$\frac{\delta_{bead}}{\delta^0_{bead}} = \frac{1}{1+\omega^2/\omega_0^2}+\frac{\omega/\omega_0}{1+\omega^2/\omega_0^2}i. \tag{2}$$

Here, the resonance frequency is given by

$$\omega_0 = \Gamma\tilde{\omega}_0, \tag{3}$$

where we define

$$\tilde{\omega}_0 = \frac{k}{b} \tag{4}$$

and

$$\Gamma = \left(1+\frac{kR}{CH_b}\right)^{-1} \tag{5}$$

The quantity CH_b/R is the effective linear restoring force constant that the bias field imposes on the DW. For large bias fields, $\Gamma\rightarrow 1$ and the bead exhibits a magneto-mechanical resonance at a frequency $\omega_0\rightarrow\tilde{\omega}_0 = k/b$. Note that a finite bias field is required for a finite resonance frequency of the coupled system.

Because the bead and DW are coupled, the latter exhibits a response that closely follows the former, given by:

$$\delta_{DW} = \Gamma\delta^0_{bead} + (1-\Gamma)\delta_{bead} \tag{6}$$

Compared to the bead response, the amplitude of the dissipative peak and the falloff of the in-phase oscillation amplitude as the system goes through resonance are smaller for the DW by a factor $(1-\Gamma)$. This factor is a measure of the dominant restoring force on the DW. In the limit of a large bias field, $\Gamma\rightarrow 1$ and the DW simply tracks the ac field with oscillation amplitude $\Gamma\delta^0_{bead}$ as the bead goes through resonance. However, at smaller H_b, magnetostatic coupling between the bead and the DW has increasing influence on the latter, leading the DW oscillation amplitude to more closely follow that of the bead as the coupled pair are driven through resonance.

This analysis suggests that resonance can be used to distinguish beads of different sizes from either the bead or the DW response to a frequency-dependent drive field.

3 Experimental and results

3.1 Optical detection and characterization of magneto-mechanical resonant dynamics

The bead-DW resonant interaction was characterized optically as shown in Fig. 2a, b. Arrays of identical $Ni_{80}Fe_{20}$ tracks on a Si(100) wafer were prepared by electron beam lithography, dc sputtering, and liftoff. Each track was 800 nm wide, 40 nm thick, and 30 μm in diameter. After patterning, the entire wafer was coated with a 70 nm thick rf-sputtered protective SiO_2 overlayer. Experiments were performed using commercial Dynabeads MyOne™ and M270 superparamagnetic beads from Dynal Biotech, with mean diameters of 1.0 μm and 2.8 μm, respectively. Beads were suspended in phosphate buffered saline (PBS) with 0.1% (v/v) Tween 20 detergent at a concentration of 3×10^5 beads/mL.

Prior to experiments, a large in-plane magnetic field was applied to coerce the tracks into an "onion" domain configuration, with two circumferential magnetic domains separated by DWs lying along the field axis.[37] A dilute suspension of SPM beads was then placed in a polydimethylsiloxane (PDMS) well on the wafer surface and sealed with a microscope cover slip. Bead capture by DW fringing fields was monitored *via* a CCD camera fitted to a custom microscope apparatus. Beads far from the tracks executed a Brownian random walk across the wafer surface, but those wandering to within ~ 10 μm of a track were abruptly drawn towards and trapped by the nearest DW. A significant number of capture events typically occurred across the array within a few minutes of bead introduction.

Magnetic fields were applied using a custom-built compact projection electromagnet capable of producing vector in-plane fields of up to 500 Oe with a bandwidth >1 kHz. For the present experiments, a dc bias field H_b was applied to fix an equilibrium

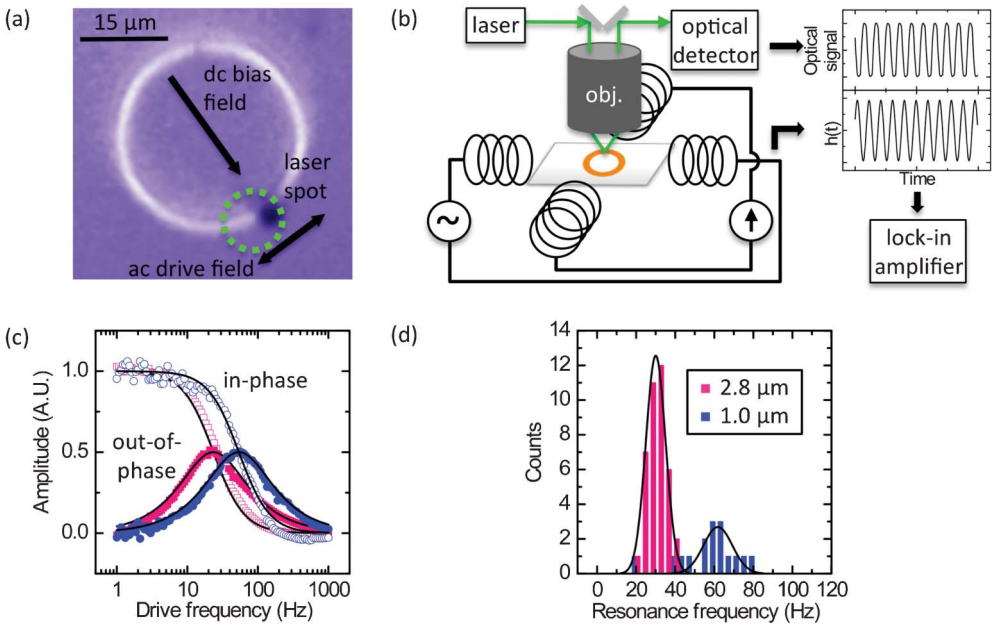

Fig. 2 Optical characterization of magneto-mechanical resonance. (a) Optical image showing a 2.8 μm diameter bead on a 30 μm outer diameter, 800 nm wide, 40 nm thick $Ni_{80}Fe_{20}$ ring, along with field configuration and probe laser spot location (dashed circle). (b) Schematic of experimental set-up for optical detection of magneto-mechanical bead resonance. Lock-in amplifier produces the signals of part (c). (c) Resonant excitation of trapped 2.8 μm diameter (squares) and 1.0 μm diameter (circles) SPM bead in aqueous environment by oscillating DW in circular magnetic track. Curves show in-phase and out-of-phase optical reflectivity signal, approximately proportional to bead oscillation amplitude. (d) Histograms of measured resonance frequencies for 2.8 μm diameter and 1.0 μm diameter beads, with mean resonance frequencies of 30.3 Hz and 58.3 Hz, respectively.

DW position, while an orthogonal in-plane ac field $h(t)$ was used to drive DW oscillations about that position (Fig. 2a).

The dynamic response of individual trapped beads was tracked using a high-bandwidth laser microprobe integrated into the imaging microscope, as shown schematically in Fig. 2b. The custom laser probe apparatus used a 532 nm solid-state laser attenuated to ~ 0.1 mW. The laser was focused and collected through a long working distance microscope objective (Mitutoyo 10× M Plan APO), and the reflected intensity was monitored with a 1 MHz bandwidth photoreceiver.

During measurement, the laser probe spot was defocused to ~ 5 μm in diameter and positioned near a bead such that bead oscillation was restricted to one side of the Gaussian spot profile (Fig. 2a). In this geometry, the detected intensity varied monotonically with bead position for small oscillation amplitudes. Fig. 2b shows an optical reflectivity trace obtained for a trapped 2.8 μm bead driven at $f = 10.5$ Hz, with $H_b = 250$ Oe and $h_0 = 20$ Oe, corresponding to a quasistatic displacement amplitude of ~ 1 μm. The trace shows a periodic decrease (increase) in reflected intensity as the bead moved into (out of) the probe spot. At this low frequency, the bead motion closely followed $h(t)$, but at higher frequencies, a phase shift between the driving field and the bead response was observed.

Response curves were generated by sweeping the ac drive frequency logarithmically through three decades, while monitoring the reflected laser intensity with a lock-in amplifier phase-locked to $h(t)$. Fig. 2c shows the in-phase and out-of-phase optical signal *versus* frequency for representative beads from the two size populations. In each case, the data are well fitted by the overdamped resonance model described above. The smaller bead exhibits a markedly higher resonance frequency, $f_0 = \frac{\omega_0}{2\pi}$, than the larger bead, as is expected from the inverse dependence of f_0 on hydrodynamic radius.

Resonance measurements were repeated for 39 large beads and 16 small beads to determine the variation of f_0 within and between these bead populations. Fig. 2d shows measured distributions in f_0 for each bead size. The data are normally distributed with a mean of 30.3 Hz for the 2.8 μm beads and 58.3 Hz for the 1.0 μm beads.

These resonance frequency data are in quantitative agreement with prediction based on the resonance model described in Section 2. The numerically-computed potential wells for the 2.8 and 1.0 μm beads in Fig. 1a, b yield fitted k values of 1.1×10^{-5} J m^{-2} and 6.8×10^{-6} J m^{-2}, respectively. Taking the drag coefficient to be of the Stokes form $b = 6\pi\eta\xi r$ for a sphere of radius r in a fluid of viscosity η, and with a near surface correction factor ξ,[38] we estimate a ratio of small to large bead resonance frequency of 1.81. The ratio of mean resonance frequency for the two bead populations closely follows prediction at a value of 1.92. Furthermore, the observed mean resonance frequency for each population is within 20% of calculation, assuming a drag enhancement of $\xi = 2.2$ for a bead dragged parallel to a surface.[38]

The standard deviation in f_0 for the 2.8 μm bead population is 4.4 Hz, corresponding to a coefficient of variation (CV) of 14.5% of the mean. For the 1.0 μm beads, the CV is somewhat larger at 24.9% of the mean. The bead size distribution specified by the manufacturer is <3% for both the MyOne™ and M270 beads. Hence, the significantly wider f_0 distributions point to a corresponding distribution in bead magnetic content. Surface adhesion between the beads and the substrate likely also contributes to variability in the measured response, and

nonspecific binding was found to be more prevalent for the 1.0 μm MyOne™, which may explain the relatively large CV for these beads. Nonetheless, these data show that the magneto-mechanical resonance can be used to robustly distinguish between these two bead populations.

3.2 Track design for microbead transport and magnetoresistive sensing

To create an infrastructure capable of trapping, transporting, and sensing all on-chip, we developed a curvilinear track[23] with a trilayer pseudo-spin-valve structure for electrical measurement of the DW resonant response. Bead capture and transport is accomplished using a mobile DW in the top (free) layer, while the bottom (fixed) layer remains uniformly magnetized and serves as a reference. In this structure, the DW position and its dynamic response can be detected electrically *via* the giant magnetoresistance effect as described below.

Device fabrication consisted of three sequential steps of lithography, deposition, and liftoff. Initial contact patterns of electron beam evaporated Ti (4 nm)/Au (100 nm) were defined by optical contact lithography on Si(100) wafers with 50 nm thermally grown SiO_2. Tracks were then patterned by electron beam lithography and liftoff, and consisted of a dc sputter-deposited $Co_{50}Fe_{50}$ (8 nm)/Cu (5 nm)/$Ni_{80}Fe_{20}$ (40 nm)/Pt (2 nm) pseudo-spin-valve stack. The $Ni_{80}Fe_{20}$ layer thickness was fixed to be the same as for the structures in Section 3.1, while the Cu thickness was optimized to minimize magnetostatic coupling between the two magnetic layers while maintaining an acceptable magnetoresistance ratio ($\sim$ 1%). Finally, Ti (2 nm)/Au (100 nm) contact lines between the tracks and the optically defined lines were patterned and deposited by electron beam lithography and evaporation, respectively. After liftoff, the entire wafer was covered by a 150 nm thick rf-sputtered SiO_2 passivation layer.

The tracks are composed of linked semi-circular segments, such that DWs are initiated and repositioned by application and rotation of an in-plane magnetic field, respectively. In this geometry, beads can be translated synchronously with DWs at a well-defined speed. Fig. 3 shows optical microscopy images of a pseudo-spin-valve curvilinear track and its transport functionality. A 2.8 μm diameter bead is shuttled right and left along the track by application of counterclockwise and clockwise field rotation, respectively. We have previously demonstrated this functionality in a single-layer track.[23] The results in Fig. 3 demonstrate that transport can likewise be achieved in the present trilayer structure, and that the overlaid electrical contacts do not impede bead motion.

The magnetic track and electrical contact lines are shown in more detail in Fig. 4a, together with a schematic illustration describing the principle of the magnetoresistive measurement of DW position (Fig. 4b). The pseudo-spin-valve stack structure consists of a non-magnetic spacer layer sandwiched between a magnetically-soft top and magnetically-hard bottom layer (Fig. 4b). In this structure, after application of a longitudinal saturation field, a DW can be introduced and manipulated in the top layer, while the bottom layer remains uniformly magnetized. In the top configuration of Fig. 4b, a longer segment of the track is antiparallel aligned, resulting in a relatively higher resistance, R^+. As the DW is repositioned by the applied in-plane field

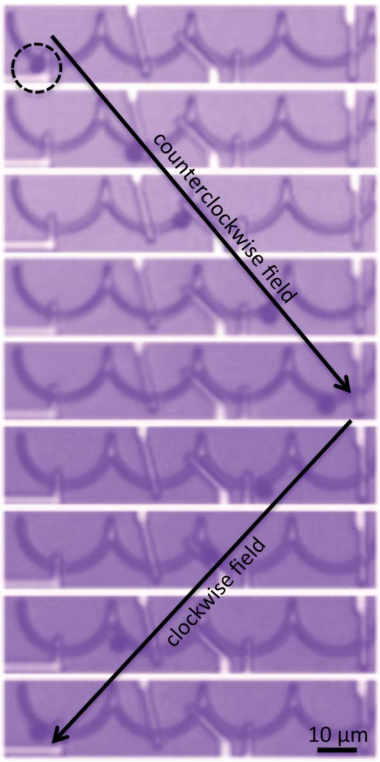

Fig. 3 Synchronous bead-DW motion along curvilinear pseudo-spin-valve track. Sequential snapshots during applied field rotation of a trapped 2.8 μm diameter SPM bead driven along a trilayer pseudo-spin-valve track of linked half-ring segments (20 μm outer diameter, 800 nm wide). Counterclockwise and clockwise field rotation results in motion to the right and the left, respectively.

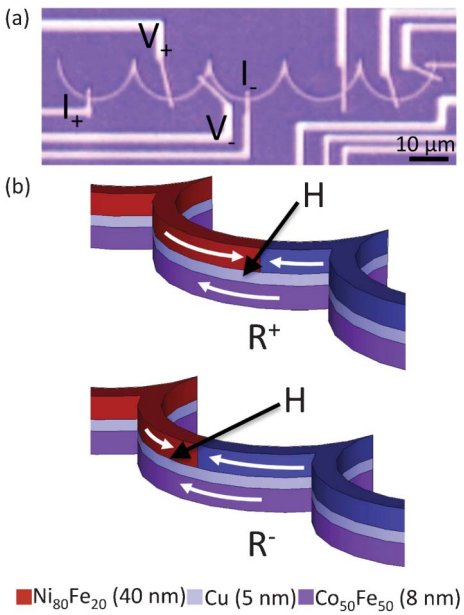

Fig. 4 Pseudo-spin-valve track for magnetoresistive sensing. (a) Curvilinear trilayer pseudo-spin-valve track for electrical detection of bead-DW magneto-mechanical resonance. Current and voltage leads indicated. (b) Change of pseudo-spin-valve track resistance as DW position in top magnetic layer is modulated by externally applied field.

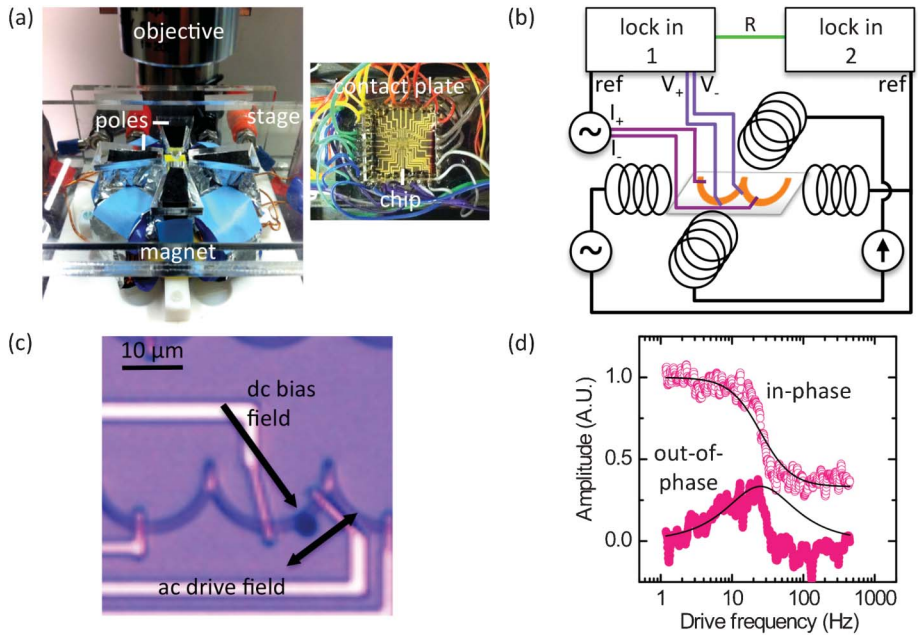

Fig. 5 Electrical measurement of DW resonance. (a, left) Magnet assembly for on-chip bead manipulation and electrical measurement. Entire assembly measures 3.5 × 6 × 2 in^3. (a, right) Chip-adapter assembly. (b) Schematic of electronics configuration for measurement of DW resonance. (c) Optical image of a 2.8 μm diameter bead trapped by DW positioned between two voltage leads of the pseudo-spin-valve curvilinear track with geometry of applied field. (d) In- and out-of-phase resonance response curves of a DW in the pseudo-spin-valve track bound to a 2.8 μm diameter bead suspended in water.

(Fig. 4b, bottom), the portion of the track that is aligned in the parallel state increases, resulting in a relatively lower resistance, R^-. Therefore, as the DW is sinusoidally driven between these two positions, the track resistance varies sinusoidally between R^+ and R^-.

Fig. 5a, b show the measurement apparatus and a schematic description of the associated electronics. The sample is placed on a stage in the plane of the custom-built magnet described above. The entire magnet assembly has a small footprint of only 3.5 × 6 in^2, suitable for point-of-care applications. Contact is made to the chip by an electrical contact adapter plate that has a center square cutout for optical access. An ac current source supplies a 100 μA, 50 kHz current to the device, and the resistance is measured by comparison of the voltage to the reference ac signal with a Stanford Research SR830 lock-in amplifier (lock-in '1').

Before measurement, a bead-DW pair is positioned in the active device area (Fig. 5c). During measurement, the excitation field is swept logarithmically from 1 to 1000 Hz. The track resistance is fed into a second SR830 lock-in amplifier (lock-in '2') phase locked with the drive field. The high output bandwidth of lock-in '1' is such that, with a maximum drive field frequency of only 1000 Hz, accurate resistance measurements can be obtained across the field sweep range. The drive frequency is swept from low to high in 600 s with a lock-in '2' time constant of 1 s such that there is sufficient sampling across the frequency spectrum.

The resonant response of a DW under these conditions is shown in Fig. 5d. The two curves show the in- and out-of-phase components of resistance, proportional to the DW oscillation amplitude, for a DW bound to a 2.8 μm diameter bead suspended in water at a concentration of 3 × 10^5 beads/mL. The predicted resonant behavior is clearly evident from these data, and the measured resonance frequency of 25 Hz is within the expected range for this bead and track geometry. The form of the measured resonance curve agrees qualitatively with eqn (6), which predicts a finite DW oscillation amplitude far above resonance. At high frequencies, the bead is effectively immobile and acts like a fixed potential well that restricts the amplitude of the field-driven DW motion but does not diminish it entirely.

Unlike the optically-measured resonance curves, the curves in Fig. 5d are asymmetric, with both the in- and out-of-phase oscillation amplitudes falling off more rapidly with frequency than the simple harmonic oscillator model predicts. This effect is most likely due to pinning of the DW by defects (edge roughness) in the track, which becomes more important when the oscillation amplitude begins to drop as the system goes through resonance. In the optical resonance experiments, a larger bias field can be used (such that $\Gamma \sim 1$ in eqn (5)), ensuring that the DW stiffly follows the drive field even in the presence of pinning. However, in the electrical measurement, it is necessary to reduce the bias field amplitude to keep $\Gamma < 1$, as per eqn (6), such that the DW is more susceptible to the magnetostatic influence of the bead. At the same time, under these conditions the DW is also more susceptible to the effects of pinning by defects in the nanotrack, and the sharper dropoff in signal past the resonant peak likely reflects more irregular DW motion as the oscillation amplitude drops. Device fabrication using a subtractive etching technique such as Ar ion milling rather than liftoff should reduce these effects by reducing edge roughness. Nonetheless, these experiments clearly demonstrate the resonant DW response due to its interaction with a trapped bead, and show that this response can be detected electrically using simple spin-valve devices.

4 Discussion

The results described above show that nanotrack-guided DWs can be used to capture, transport, and interrogate the physical properties of individual magnetic microbeads in a host fluid. DW-based devices therefore offer a possible means to realize a digital lab-on-a-bead platform, where biotarget capture occurs on the surface of microbeads rather than on the surface of the chip, and sensed biomaterials could be subsequently transported or sorted using mobile DW traps. Biosensor chips based on magneto-mechanical resonant sensing would not require pre-functionalization, but would be generic in their operation. Specific detection targets would be chosen by the end user at the point-of-use through selection of beads with the desired surface chemistry. Moreover, this DW-based approach offers added transport functionality that could augment or eliminate the need for, *e.g.*, microfluidic actuation and associated hardware.

We have demonstrated that the magneto-mechanical resonance can be used to reliably discriminate between commercial microbead populations with substantial differences in their hydrodynamic radii. The ultimate goal of lab-on-a-bead sensing systems is to allow detection of analyte hybridization to functionalized beads, typically through DNA-cDNA recognition, or through an immunoassay recognition. Based on the results above, an increase in hydrodynamic radius of several hundred nm (significantly larger than the typical size of individual biomolecules) would be required to statistically separate decorated from undecorated beads in a population of 2.8 μm beads. However, there are several biorecognition strategies that would be compatible with the demonstrated sensitivity to hydrodynamic radius afforded by DW-based magneto-mechanical resonant sensing. In Strömberg *et al.*,[31,32] Brownian relaxation biodetection was based on the formation of clusters of magnetic beads bound by a network of DNA or antibodies using a volume-amplified approach. These clusters indicated the presence of an analyte *via* a change in the Brownian relaxation frequency as compared to unclustered magnetic beads. The approach described here could offer a means to detect chemically-bound magnetic clusters in a chip-based DW device through this same biochemical recognition strategy. Alternatively, bead-on-bead sandwich assays have been successfully employed for, *e.g.*, protein detection,[39–41] and offer a possible means to realize biosensing in DW-based devices. In Jans *et al.*,[41] magnetic microbeads were used for target protein capture, and secondary Au nanoparticles hybridized with the capture microbeads were used for optical signal transduction. An analogous approach could be used for biomolecule detection in DW-based devices, whereby secondary bead hybridization to magnetic capture beads in the presence of a target analyte would lead to a detectible change in hydrodynamic radius. Finally, in cases in which the target analyte is a discrete object such as a cell or bacterium, on-the-fly detection in chip-based devices has been demonstrated by labeling the target with magnetic nanoparticles. For such applications, DW-based transport conduits could simultaneously capture, transport, and sense the presence of the analyte through its hydrodynamic characteristics.

5 Conclusion

By harnessing the strong gradient field of DWs and using specifically designed track structures, we have developed a SPM bead transport scheme that integrates single bead manipulation and metrology. The bead-DW magnetostatic interaction leads to a distinct magneto-mechanical resonance that is quantitatively well-described by an overdamped harmonic oscillator model. We have demonstrated that the magneto-mechanical resonance can be used to distinguish bead populations based on their size, and that the resonant behavior of the coupled bead-DW system can be sensed electrically using simple spin-valve devices. The integration of single-bead capture, transport and metrology on-chip is a step toward multifunctional devices for lab-on-a-bead technologies.

Acknowledgements

This work was supported by the MIT Deshpande Center for Technological Innovation, the MIT Center for Materials Science and Engineering, and the Charles E. Reed Faculty Initiatives Fund. D. M. acknowledges support through the MIT Undergraduate Research Opportunities Program. Device fabrication was carried out at the MIT NanoStructures Laboratory. The authors gratefully acknowledge David Bono and Mike Tarkanian for technical assistance.

References

1 D. R. Baselt, G. U. Lee, M. Natesan, S. W. Metzger, P. E. Sheehan and R. J. Colton, *Biosens. Bioelectron.*, 1998, **13**, 731–739.
2 R. Edelstein, C. Tamanaha, P. Sheehan, M. Miller, D. Baselt, L. Whitman and R. Colton, *Biosens. Bioelectron.*, 2000, **14**, 805–813.
3 L. Lagae, R. Wirix-Speetjens, J. Das, D. Graham, H. Ferreira, P. P. F. Freitas, G. Borghs and J. De Boeck, *J. Appl. Phys.*, 2002, **91**, 7445–7447.
4 Q. Pankhurst, J. Connolly, S. Jones and J. Dobson, *J. Phys. D: Appl. Phys.*, 2003, **36**, R167–R181.
5 M. Gijs, *Microfluid. Nanofluid.*, 2004, **1**, 22–40.
6 H. Lee, A. Purdon and R. Westervelt, *Appl. Phys. Lett.*, 2004, **85**, 1063–1065.
7 K. Gunnarsson, P. Roy, S. Felton, J. Pihl, P. Svedindh, S. Berner, H. Lidbaum and S. Oscarsson, *Adv. Mater.*, 2005, **17**, 1730–1734.
8 B. Yellen, O. Hovorka and G. Friedman, *Proc. Natl. Acad. Sci. U. S. A.*, 2005, **102**, 8860–8864.
9 R. Derks, A. Dietzel, R. Wimberger-Friedl and M. Prins, *Microfluid. Nanofluid.*, 2007, **3**, 141–149.
10 J. Dobson, *Nat. Nanotechnol.*, 2008, **3**, 139–143.
11 C. Liu, T. Stakenborg, S. Peeters and L. Lagae, *J. Appl. Phys.*, 2009, **105**, 102014.
12 L. Johansson, K. Gunnarsson, S. Bijelovic, K. Eriksson, A. Surpi, E. Göthelid, P. Svedlindh and S. Oscarsson, *Lab Chip*, 2010, **10**, 654–661.
13 J. Llandro, T. J. Hayward, D. Morecroft, J. A. C. Bland, F. J. Castaño, I. A. Colin and C. A. Ross, *Appl. Phys. Lett.*, 2007, **91**, 203904.
14 S. X. Wang and G. Li, *IEEE Trans. Magn.*, 2008, **44**, 1687–1702.
15 V. C. Martins, F. A. Cardoso, J. Germano, S. Cardoso, L. Sousa, M. Piedade, P. P. Freitas and L. P. Fonseca, *Biosens. Bioelectron.*, 2009, **24**, 2690–2695.
16 R. S. Gaster, L. Xu, S.-J. Han, R. J. Wilson, D. A. Hall, S. J. Osterfeld, H. Yu and S. X. Wang, *Nat. Nanotechnol.*, 2011, **6**, 314–320.
17 P. Vavassori, V. Metlushko, B. Ilic, M. Gobbi, M. Donolato, M. Cantoni and R. Bertacco, *Appl. Phys. Lett.*, 2008, **93**, 203502.
18 G. Vieira, T. Henighan, A. Chen, A. Hauser, F. Yang, J. Chalmers and R. Sooryakumar, *Phys. Rev. Lett.*, 2009, **103**, 128101.

19 M. Donolato, P. Vavassori, M. Gobbi, M. Deryabina, M. F. Hansen, V. Metlushko, B. Ilic, M. Cantoni, D. Petti, S. Brivio and R. Bertacco, *Adv. Mater.*, 2010, **22**, 2706–2710.
20 M. T. Bryan, K. H. Smith, M. E. Real, M. A. Bashir, P. W. Fry, P. Fischer, Mi-Young Im, T. Schrefl, D. A. Allwood and J. W. Haycock, *IEEE Magn.s Lett.*, 2010, **1**, 1500104.
21 G. Ruan, G. Vieira, T. Henighan, A. Chen, D. Thakur, R. Sooryakumar and J. O. Winter, *Nano Lett.*, 2010, **10**, 2220–2224.
22 M. Donolato, A. Torti, N. Kostesha, M. Deryabina, E. Sogne, P. Vavassori, M. F. Hansen and R. Bertacco, *Lab Chip*, 2011, **11**, 2976–2983.
23 E. Rapoport and G. S. D. Beach, *Appl. Phys. Lett.*, 2012, **100**, 082401.
24 B. T. Dalslet, C. D. Damsgaard, M. Donolato, M. Strømme, M. Strömberg, P. Svedlindh and M. F. Hansen, *Lab Chip*, 2011, **11**, 296–302.
25 M. Donolato, E. Sogne, B. T. Dalslet, M. Cantoni, D. Petti, J. Cao, F. Cardoso, S. Cardoso, P. P. Freitas, M. F. Hansen and R. Bertacco, *Appl. Phys. Lett.*, 2011, **98**, 073702.
26 E. Rapoport and G. S. D. Beach, *J. Appl. Phys.*, 2012, **111**, 07B310.
27 R. Kotitz, W. Weitschies, L. Trahms, W. Brewer and W. Semmler, *J. Magn. Magn. Mater.*, 1999, **194**, 62–68.
28 J. Connolly and T. G. St Pierre, *J. Magn. Magn. Mater.*, 2001, **225**, 156–160.
29 A. P. Astalan, F. Ahrentorp, C. Johansson, K. Larsson and A. Krozer, *Biosens. Bioelectron.*, 2004, **19**, 945–951.
30 C.-Y. Hong, W. S. Chen, Z. F. Jian, S. Y. Yang, H. E. Horng, L. C. Yang and H. C. Yang, *Appl. Phys. Lett.*, 2007, **90**, 074105.
31 M. Strömberg, J. Göransson, K. Gunnarsson, M. Nilsson, P. Svedlindh and M. Strømme, *Nano Lett.*, 2008, **8**, 816–821.
32 M. Strömberg, T. Zardán Gómez de la Torre, J. Göransson, K. Gunnarsson, M. Nilsson, P. Svedlindh and M. Strømme, *Anal. Chem.*, 2009, **81**, 3398–3406.
33 G. A. Prinz, *Science*, 1998, **282**, 1660–1663.
34 M. J. Donahue and D. G. Porter, *OOMMF User's Guide Version 1.0*, National Institute of Standards and Technology, Gaithersburg, MD, 1999.
35 Y. Nakatani, A. Thiaville and J. Miltat, *J. Magn. Magn. Mater.*, 2005, **290–291**, 750–753.
36 We have calculated the binding energy under application of an in-plane magnetic field transverse to the track and find no significant change, due to the predominantly out-of-plane gradient of the DW stray field.
37 C. A. Ross, F. J. Castano, W. Jung, B. G. Ng, I. A. Colin and D. Morecroft, *J. Phys. D: Appl. Phys.*, 2008, **41**, 113002.
38 J. Happel and H. Brenner, *Low Reynolds number hydrodynamics: with special applications to particulate media*, Martinus Nijhoff Publishers, 1983.
39 J. M. Nam, C. S. Thaxton and C. A. Mirkin, *Science*, 2003, **301**, 1884–1886.
40 Y. H. Tennico, D. Hutanu, M. T. Koesdjojo, C. M. Bartel and V. T. Remcho, *Anal. Chem.*, 2010, **82**, 5591–5597.
41 H. Jans, K. Jans, P.-J. Demeyer, K. Knez, T. Stakenborg, G. Maes and L. Lagae, *Talanta*, 2011, **83**, 1580–1585.